Magnetized Topological Insulator Multilayers

Chao Lei[a], **Shu Chen**[a,b]**, and Allan H. MacDonald**[a,1]

[a]Department of Physics, The University of Texas at Austin, Austin, Texas 78712, USA; [b]Department of Physics, Shanghai University, Shanghai 200444, China

We discuss the magnetic and topological properties of bulk crystals and quasi-two-dimensional thin films formed by stacking intrinsic magnetized topological insulator (for example Mn(Sb$_x$Bi$_{1-x}$)$_2$X$_4$ with X = Se,Te) septuple layers and topological insulator quintuple layers in arbitrary order. Our analysis makes use of a simplified model that retains only Dirac-cone degrees of freedom on both surfaces of each septuple or quintuple layer. We demonstrate the model's applicability and estimate its parameters by comparing with *ab initio* density-functional-theory(DFT) calculations. We then employ the coupled Dirac cone model to provide an explanation for the dependence of thin-film properties, particularly the presence or absence of the quantum anomalous Hall effect, on film thickness, magnetic configuration, and stacking arrangement, and to comment on the design of Weyl superlattices.

Topological Superlattice | Magnetized Topological Insulator | Density Functional Theory | Quantum Anomalous Hall Effect | Weyl Semimetal

Topological insulator (TI) thin films in which time-reversal symmetry is broken by magnetic order(1) have long been recognized as a promising platform for the interplay between transport and magnetic properties that powers spintronics. Indeed the quantum anomalous Hall (QAH) effect, a high point of topological spintronics characterized by dissipationless transport, was first observed(2, 3) in magnetic topological insulator (MTI) thin films with ferromagnetic order, and strong magneto-electric response properties are expected in antiferromagnetic TI films(4–6). MTIs were first produced simply by doping (Sb$_x$Bi$_{1-x}$)$_2$X$_3$ TI thin films with magnetic elements. However, disorder, thought to be due mainly to inhomogeneity of the magnetic dopants(7), leads to complex magnetic order in these systems. As a consequence the QAH effect appears only at extremely low temperatures, for example only at ∼ 30 mK in Cr-doped Bi$_2$Te$_3$, even though the Curie temperature is ∼ 15K(3). For this reason the recent identification(8) of the Mn(Sb$_x$Bi$_{1-x}$)$_2$X$_4$ family of layered van der Waals materials, which can be viewed as MTIs that have magnetic moments on an ordered lattice, is a promising advance.

Important progresses have been made in understanding the bulk and epitaxial thin film properties of this family of materials, both theoretically(8–13) and experimentally(14–31). The quantum anomalous Hall effect has now been observed in the presence of a relatively weak magnetic fields ∼ 5T for thicknesses ranging from 3-10 septuple layers(21, 23, 29), and large (almost quantized) anomalous Hall effects have been observed in the absence of an external magnetic field in high-quality five-septuple-layer MnBi$_2$Te$_4$ films(23), all at temperatures exceeding 1K. The ratio of the quantum anomalous Hall temperature to the magnetic ordering temperature, ∼ 20K, is much higher(29) than in doped MTI films. Some (10, 16, 18, 32) (but not all (26–28, 33)) photoemission experiments have identified the large surface state gaps ∼ 100meV that are generally expected (10, 15) theoretically in MTIs.

Mn(Sb$_x$Bi$_{1-x}$)$_2$X$_4$ is a layered material composed of seven-layers X-(B,Sb)-X-Mn-X-(Bi,Sb)-X units that are coupled by weak van der Waals interactions. These septuple layers may be viewed as (Bi,Sb)$_2$X$_3$ quintuple layers in which the middle X layer is replaced by an X-Mn-X trilayer. In agreement with theoretical predictions(9, 12), neutron scattering measurements (17, 26, 30) show that bulk MBX has A-type antiferromagnetic order with Mn ions ordered ferromagnetically within each septuple layer and antiferromagnetically between adjacent septuple layers. Because the antiferromagnetic interactions between septuple layers are weak, the Mn layer moments in thin films can be aligned by magnetic fields ∼ 5 Tesla. Thin films can be obtained either by epitaxial growth or by mechanical exfoliation from bulk crystals (8, 30, 31, 34–39). Magnetic fields establish quantum Hall effects in thin films not by establishing Landau quantization, but by changing the magnetic configuration from antiferromagnetic to ferromagnetic through overcoming the weak interlayer exchange interactions (21, 23, 29).

In this paper, we develop a simple model that can be used to address the properties of thin films and bulk crystals formed by stacking Mn(Sb$_x$Bi$_{1-x}$)$_2$X$_4$ septuple layers and (Sb$_x$,Bi$_{1-x}$)$_2$X$_3$ quintuple layers in arbitrary order. The model contains only Dirac cone degrees of freedom on each surface of each septuple or quintuple layer. By comparing with *ab initio* density-functional-theory (DFT) calculations we are able to establish that this highly simplified description is usually accurate, and also to fix values of the model's material-dependent parameters. The advantages of the simplified model are that it facilitates the descriptions of crystals with complex stacking sequences and thin-films containing many layers, and more importantly that it allows trends in magnetic and topological

Significance Statement

Topological insulators like the van der Waals crystal Bi$_2$Te$_3$ have Dirac-cone surface states protected by time-reversal symmetry (TRS). Weak magnetic order in topological insulator thin films can lead to the quantum anomalous Hall effect (QAHE), which was first realized by magnetic doping of topological insulators to establish a fragile ferromagnetic state. Recent work has established MnBi$_2$Te$_4$ as a structurally ordered magnetic topological insulator. We report on a theoretical study of thin films formed from MnBi$_2$Te$_4$ and Bi$_2$Te$_3$ building blocks that employs a simplified model validated by *ab initio* density-functional-theory. We use it to shed light on the dependence of the quantum anomalous Hall effect on film thickness, magnetic configuration, the stacking sequences of the van der Waals coupled building blocks, and bulk electronic structure.

properties across the family of materials to be recognized and understood. Important materials variations include changes in the Sb fraction x on the pnictogen sites, substitutions of X=S,Se,Te on the different chalcogen sites, and growth controlled defect concentrations. Our model can also be used as a starting point for theories that account for gating electric fields, external magnetic fields, disorder, and other perturbations that are difficult to describe using *ab initio* approaches.

In this paper we focus on Bi_2X_3 and $MnBi_2X_4$ with X=Se,Te, which have received greatest attention to date. We find that bulk ferromagnetic $MnBi_2X_4$ (MBX) is a nearly ideal Weyl semimetal, that thin-film ferromagnets are two-dimensional Chern insulators with Chern numbers that grow and gap sizes that decline with film thickness, and that antiferromagnetic thin films with sufficiently large odd layer numbers are Chern insulators with Chern number $|C| = 1$. We further find that ferromagnetic $[MnBi_2X_4]_M[Bi_2X_3]_N$ superlattices formed by inserting non-magnetic quintuple layers in the stack are ordinary insulators for M/N smaller than about 3, but become Weyl semimetals for larger M/N. For superlattices with (M,N) = (1,1), there is a large chance to acheive a Weyl semimetal phase with $MnBi_2Te_4$ as magnetic topological insulator layers and Bi_2Se_3, Bi_2Sb_3, or Sb_2Te_3 as topological insulator layers.

Coupled Dirac Cone Model

We construct a model for a magnetized topological insulator multilayer by including Dirac cone degrees of freedom not only on the surface layers(40, 41), but also on the top and bottom of each magnetic septuple layer and non-magnetic quintuple layer as illustrated in Fig. 1. We allow for arbitrary stacking of magnetic and non-magnetic layers either to form a thin film, or if repeated to form a bulk crystal.
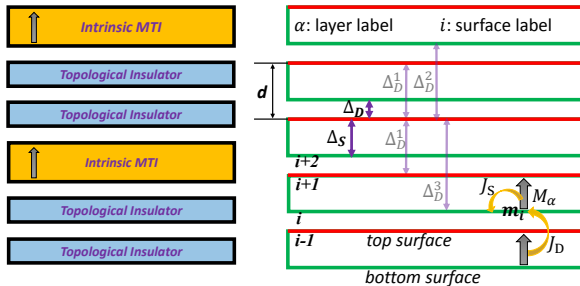

Fig. 1. Coupled Dirac Cone Model: (Left Panel) Magnetized topological insulator multilayers composed of M magnetic septuple layers and N non-magnetic quintuple layers. (Right panel) Dirac cone model in which Dirac cones localized on the top and bottom of each layer are hybridized with remote Dirac-cones and altered by exchange interactions with the local moments present in the magnetic layers.

We allow for exchange interactions with the Mn local moments and arbitrary spin-independent hybridization between different surfaces, denoting the hopping parameter between the ith surface and the jth surface by Δ_{ij}. The Hamiltonian is therefore:

$$H = \sum_{\mathbf{k}_\perp, ij} \left[\left((-)^i \hbar v_D (\hat{z} \times \sigma) \cdot \mathbf{k}_\perp + m_i \sigma_z \right) \delta_{ij} + \Delta_{ij}(1 - \delta_{ij}) \right] c^\dagger_{\mathbf{k}_\perp i} c_{\mathbf{k}_\perp j} , \quad [1]$$

where spin-labels have been left implicit, i and j are Dirac cone labels with even integers reserved for layer bottoms and odd for layer tops, $\hbar$ is the reduced Planck constant, and v_D is the velocity of the Dirac cones. The most important hybridization parameters, hopping within the same layer (Δ_S) and hopping across the van der Waals gap between adjacent layers (Δ_D), are highlighted in Fig. 1. The mass gaps m_i of the individual Dirac cones result from exchange interactions with Mn local moments and break time reversal symmetry:

$$m_i = \sum_\alpha J_{i\alpha} M_\alpha, \quad [2]$$

where α is a layer label. We limit our attention here to the case of magnetization perpendicular to the van der Waals layers so that $M_\alpha = \pm 1$ specifies the sense of magnetization on layer α if it is magnetic, and $M_\alpha = 0$ on non-magnetic layers. Each Dirac cone can have two nearby Mn layers, one from the same layer with exchange splitting J_S and one from the adjacent layer with exchange splitting J_D, shown as in Fig. 1), if these layers are magnetic. In our surveys of MTI superlattice properties we retain only Δ_S, Δ_D, J_S and J_D, which are normally dominant, as model parameters, the model allows different values of Δ_S in TI and MTI layers, and allows Δ_D at magnetic/non-magnetic heterojunctions to differ its value at magnetic/magnetic or non-magnetic/non-magnetic heterojunctions.

The model simplifies when only one type of layer is present. When that layer is magnetic and the magnetic configuration is ferromagnetic, our model reduced to the topological insulator multilayer model proposed by Burkov and Balents (42). Instead of inserting a normal insulating layer between magnetic topological insulator layers to form a flexible three-dimensional system, as imagined in Ref. (42), in this model the coupling between Dirac cones on different layers is across the van der Waals gap. As we discuss below, some of the flexibility that would be associated with non-magnetic spacer layers of variable thickness, can be recovered by inserting non-magnetic TI layers between magnetic TI layers.

Comparison to DFT calculations

The relevance of the model that retains only Dirac-cone degrees of freedom to realistic systems can be tested by comparing with *ab initio* density-functional-theory (DFT) electronic structure calculations, which we performed using a LDA+U approximation(43) with U = 5.25 eV on Mn sites.

Non-Magnetic. As a first test of the model, we examine the bands of bulk Bi_2Se_3 as estimated by DFT. We find that we can obtain a reasonable approximation to the DFT bands retaining only the hybridization parameters Δ_S for hopping within the same layer, and Δ_D for hopping to the adjacent surface of the adjacent layer. The fit can be improved by adding Δ_D^1, for hopping to the same surface of the adjacent layer. Retaining only these three parameters the model predicts two spin-degenerate bands along the Γ to Z line in the Brillouin zone with dispersions

$$E(k_z) = \pm\sqrt{\Delta_S^2 + \Delta_D^2 + 2\Delta_S\Delta_D \cos k_z d} + 2\Delta_D^1 \cos k_z d, \quad [3]$$

with d the distance between layer centers and k_z the momentum along the Γ-Z line. The corresponding DFT bands are

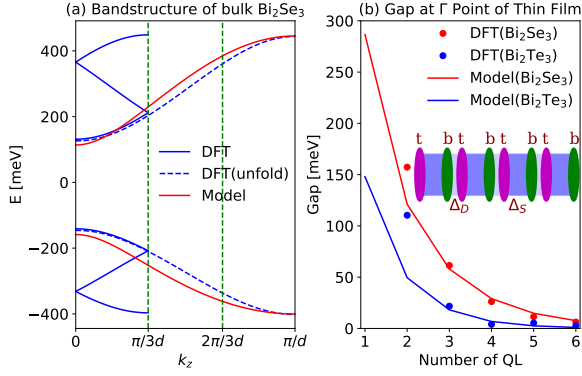(a) Bandstructure of bulk Bi$_2$Se$_3$ (b) Gap at Γ Point of Thin Film

Fig. 2. Band structure of Bi$_2$Se$_3$ along the Γ to Z line from DFT calculations and the Dirac cone model. (a) The blue line is the result from DFT calculations. Since the bulk Bi$_2$Se$_3$ layer stacking arrangement has three quintuple layers per unit cell, the DFT bands must be unfolded to the larger Brillouin zone. Fitting the bulk DFT band dispersion from Γ to Z yields Δ_S = 143 meV, Δ_D = -280 meV and Δ_D^1 = -11 meV. The sign of Δ_S has been fixed by noting that the single-layer conduction band state at Γ has greater weight in the middle of the layer than the valence band state. The corresponding Bi$_2$Te$_3$ fit yields Δ_S = 74 meV, Δ_D = -200 meV, and Δ_D^1 = -10 meV. (b) Comparison between DFT and Dirac cone models for thin film gaps at the two-dimensional Γ point *vs.* layer number. In the displayed scale, the gaps from DFT calculations are out of the displayed range, it is around 847 meV for Bi$_2$Se$_3$ and around 488 meV for Bi$_2$Te$_3$. The Dirac cone models were obtained by fitting to the bulk band dispersion. In the schematic illustration of the Dirac cone bonding network, t/b label the top/bottom surfaces of individual layers represented by magenta/green ellipses and the purple and grey links represent hopping within and between layers.

Table 1. Model parameters for MnBi$_2$X$_4$(X = Se,Te) in units of meV. For the column labelled DFT/EXP we use the experimentally available value of the antiferromagnetic state gap, and DFT calculation results for quantities that were not available from experiment.

Magnetic Configuration	MBS (Model)	MBS (DFT/Exp.)	MBT (Model)	MBT (DFT/Exp.)
Δ_S	190	–	84	–
Δ_D	-232	–	-127	–
J_S	32	–	36	–
J_D	25	–	29	–
E_{gap}^Γ(AF)	85	$\simeq$100	86	50-200
E_{gap}^Γ(FM)	30	$\simeq$23	44	12

illustrated in Fig. 2. Because of details of the stacking arrangements that are not captured by the simplified model, the Bi$_2$Se$_3$ lattice used in the DFT calculations repeats only after three layers, instead of after a single layer. Nevertheless we find excellent agreement between the two sets of bulk bands once the DFT bands are unfolded to the larger Brillouin-zone. The property that the gap between the low energy bands is larger at Z than at Γ implies that Δ_S and Δ_D have opposite signs. The parameter Δ_D^1 is added to account for the small difference between the average of the DFT conduction and valence band energies at Γ and Z. The model band energies at the Γ point ($k_z d = 0$) and the Z point ($k_x d = \pi$) are respectively $\pm|\Delta_S + \Delta_D| + 2\Delta_D^1$ and $\pm|\Delta_S - \Delta_D| - 2\Delta_D^1$. Fitting to these four energies we obtain Δ_S = 143 meV, Δ_D = -280 meV and Δ_D^1 = -11 meV. The corresponding fitted parameters for Bi$_2$Te$_3$ are Δ_S = 74 meV, Δ_D = -200 meV, and Δ_D^1 = -10 meV. The property that $|\Delta_D|$ is larger than $|\Delta_S|$, which is responsible for band inversion at Γ and hence for the non-trivial band topology, is not surprising since the former hopping parameter is across a narrow van der Waals gap whereas the latter is across a wider quintuple layer. As seen in Fig. 2 (a) the unfolded DFT bands are in excellent agreement with this simple model.

Using these parameters estimated from the bulk bands at Γ and Z, we calculated the gap at the two-dimensional Γ point for Bi$_2$Se$_3$ and Bi$_2$Te$_3$ thin films with thicknesses ranging from 1 to 6 quintuple layers. As illustrated in Fig. 2 (b), the gaps of thin films from the simplified model are in good agreement with DFT results (shown with red and blue dots), except in the single quintuple layer case for Bi$_2$Se$_3$ and in the single and double quintuple layer cases for Bi$_2$Te$_3$. For the latter material the Dirac point lies in the valence bands instead of in the bandgap. This good agreement supports a physical

picture in which the bulk gap is due to the hybridization of the Dirac cones network. The thin film gap is small because the top(bottom) Dirac cone of the top(bottom) layer has no hybridization partner from adjacent layers (shown as inserted plot in Fig. 2 (b)). The thin film gap is due to hopping between surface layer Dirac cones via hybridized, and therefore gapped, Dirac cones in the interior. Because Δ_D^1 is small compared to Δ_D we include only Δ_S and Δ_D in the following analysis. The model's Dirac velocity parameter is estimated from the dependence of the DFT bands on in-plane momenta. (See Fig.S1 and Table S1 in the SI Appendix.)

Magnetic. We now turn to the magnetic case, starting with bulk MnBi$_2$Se$_4$(MBS) and MnBi$_2$Te$_4$(MBT). Below we refer to the magnetic configuration in which all magnetic layers are aligned as ferromagnetic. The ground state is antiferromagnetic, but because magnetic interactions between different van der Waals layers are extremely weak, the ferromagnetic configuration can be realized by applying a relatively modest external magnetic field. For the ferromagnetic configuration the exchange energies are the same in every layer and the model band energy dispersion along the Γ to Z line is

$$E(k_z) = \pm\sqrt{\Delta_S^2 + \Delta_D^2 + 2\Delta_S\Delta_D \cos k_z d} \pm m_F, \quad [4]$$

where the ferromagnetic exchange splitting is $m_F = J_S + J_D$ is the sum of the on-layer (J_S) and neighboring-layer (J_D) exchange interactions. The energies at $k_z d = 0$ and $k_z d = \pi$ are

$$E_\Gamma = \pm(\Delta_S + \Delta_D) \pm m_F$$
$$E_Z = \pm(\Delta_S - \Delta_D) \pm m_F. \quad [5]$$

Because m_F depends only on $J_S + J_D$ we must consider other magnetic configurations in order to fit J_S and J_D independently. For the antiferromagnetic configuration the exchange splitting $m_{AF} = J_S - J_D$ alternates in sign from layer to layer and the gap between conduction and valence bands at the Γ point is

$$E_{gap}^{AF} = 2(\sqrt{\Delta_D^2 + m_{AF}^2} - \Delta_S). \quad [6]$$

By comparing these expressions with the DFT band dispersions of bulk MnBi$_2$X$_4$(X = Se,Te), we extract the model parameters summarized in Table S1.

The Γ to Z band dispersions calculated with these model parameters for the ferromagnetic configuration are illustrated in Fig. 3(a). Because the Γ-point gaps, around 30 meV for MBS and around 44 meV for MBT, are inverted by the exchange splitting m_F, the spin-splitting closes at a finite value of k_z, as noted previously (12, 13), generating a simple Weyl semimetal

MacDonald *et al.*

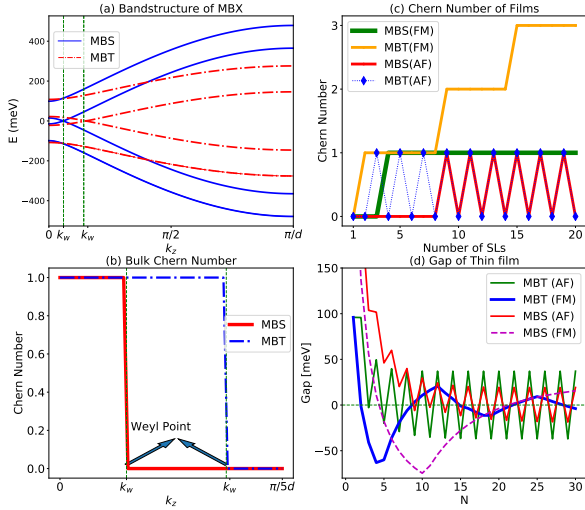PNAS | September 29, 2020 | vol. XXX | no. XX | 3

Fig. 3. (a) Bulk band dispersion of ferromagnetic MBX calculated from the Dirac cone model with the DFT-extracted parameters summarized in Table S1. Ferromagnetic $MnBi_2X_4$(X=Se,Te) is a Weyl semimetal, with the Weyl point located at $k_z = \pm k_w$ where $k_w \approx 3\pi/50d$ for MBS and $k_w \approx 3\pi/20d$ for MBT. (b) Dirac-cone model k_z-dependent 2D Chern numbers for bulk MBX calculated from the model, showing jumps from 1 to 0 at the Weyl points. (c) 2D Chern numbers of thin-film MBX calculated from the Dirac-cone model which show that the Chern numbers of ferromagnetic MBX jump to no-zero values beyond four septuple layers thickness for MBS and 2 septuple layers for MBT. The antiferromagnetic configurations have non-zero Chern numbers for odd-septuple-layer films when the thickness is larger than 8 layers for MBS and 2 layers for MBT. (d) Gap of thin-film MBX at the 2D-Γ point as a function of the number of septuple layers.

(44) with only two Weyl points. The model bands are in good agreement overall with the DFT results, although the small Γ-point gaps are even smaller in our DFT calculations, which yield 23 meV for MBS and 12 meV for MBT. The role of longer-range hopping parameters Δ_D^n, which are responsible for a velocity magnitude difference between the crossing bands at the Weyl point, is addressed in SI Appendix, Fig. S2 by DFT calculations but dropped in the qualitative phase-diagram discussions below since they are $\sim$ several meV and have little influence on the positions of Weyl points (k_w), thin film AHEs, or 2D-Γ point thin film gap (SI Appendix, Fig. S3) trends. The bulk antiferromagnetic gaps calculated from this model are around 85 meV for MBS and 86 meV for MBT, compared to gaps estimated experimentally that vary from 50 meV to 200 meV(10, 16, 30, 45).

In Fig. 3(b) we plot 2D Chern numbers obtained by integrating the Berry curvature over k_x and k_y as a function of k_z, which are non-zero between the Weyl points at $k_z = \pm k_w$. The Weyl momentum k_w is non-zero for $m_F > |\Delta_D| - |\Delta_S|$ and moves from Γ to Z with increasing m_F, reaching π/d when $m_F = |\Delta_D| + |\Delta_S|$. The bulk Hall conductivity per layer is (46) $k_w/(\pi/d)e^2/h$. Since the exchange interactions m_F in MBX are larger than $|\Delta_D| - |\Delta_S|$, but quite small compared to $|\Delta_S| + |\Delta_D|$, the Hall conductivity per septuple layer in bulk ferromagnetic MBX is small compared to the quantum value e^2/h.

In Fig. 3 (c) we plot the total Chern numbers of thin films with ferromagnetic and antiferromagnetic configurations as a function of the number of septuple layers in the film. For ferromagnetic configurations, the thin films have zero Chern number for thicknesses up to a critical number of septuple

layers, which is 4 for MBS and 2 for MBT. As the thickness increases the Chern numbers increase indefinitely, increasing by one for every $\sim \pi/d/k_w$ added septule layers so that the quantized Hall conductivity of very thick films approaches the bulk value when normalized per layer (See SI Appendix, Fig. S4). As the Chern number increases the energy gaps tend to decrease, as illustrated in Fig. 3 (d), where we have assigned a negative sign to the gap for odd integer Chern numbers. The oscillating gap size simply reflects the size-quantization of the bulk Weyl semimetal bands, as detailed in SI Appendix, Fig. S5. The behavior of antiferromagnetic configurations is quite distinct. Here the Chern numbers are non-zero only for odd numbers of septuple layers and, in that case, only when a critical film thickness equal to 2 septuple layers for MBT and 8 septuple layers for MBS is exceeded. The antiferromagnetic configuration gaps are identical for even and odd numbers of layers in the thick film limit. (See SI Appendix, Fig. S5). These semi-analytic predictions of the Dirac cone model are consistent with recent experiments(21, 23, 29) which have, in particular, shown that for MBT films the total Chern number jumps from 1 to 2 when the thickness reaches nine(29) septuple layers.

Superlattice Phase Diagrams

The van der Waals character of MBX materials allows for property variation by changing the stacking sequence of magnetic septuple and non-magnetic quintuple layers(30, 35, 37–39). Importantly, the magnetic field needed to convert between antiferromagnetic and ferromagnetic stacking arrangements can be reduced simply by inserting non-magnetic quintuple spacers between the magnetic septuple layers. When magnetic and non-magnetic layers are simply alternated, for example, it has been shown experimentally that the magnetic field needed to convert to a ferromagnetic configuration is reduced from $\sim 5T$ to $\sim 0.22T$(30).

We consider the family of bulk crystals in which a template with M $MnBi_2X_4$ septuple layers and N Bi_2X_3 quintuple layers is repeated. Several of these superlattices have already been realized experimentally including $(M,N) = (1,1)$ $(MnBi_4Se_7)$ (30, 37–39),$(M,N) = (1,2)$ $(MnBi_6Se_{10})$ (37, 39), and $(M,N) = (1,3-6)$ ($MnBi_8Se_{13}$, $MnBi_{10}Se_{16}$, and $MnBi_{12}Se_{19}$) (39). In Fig. 4 we summarize the energy gaps and topological phases of ferromagnetic configuration $(MnBi_2X_4)_M/(Bi_2X_3)_N$ superlattices. We find that the energy gap is mainly determined by the ratio of magnetic to non-magnetic layers M/N, and is less dependent on the order of the layers. For example, when we set $\Delta_S^{MTI} = \Delta_S^{TI}$, we find that M/N larger than around 3 leads to bulk Weyl semimetals. Decreasing $\Delta_S^{MTI}/\Delta_S^{TI}$ favors Weyl semimetal phases with a decrease of around $\pm 10\%$ reducing the critical M/N ratio to 2. We therefore expect that stronger hybridization between surface states within the non-magnetic topological insulator layers favors Weyl semimetals. Among $(M,N) = (1,1)$ superlattices, candidates include $MnBi_2Te_4$ combined with Bi_2Se_3, Bi_2Sb_3, or Sb_2Te_3, which are estimated to have stronger same layer hybridization than Bi_2Te_3 according to the DFT calculations summarized in SI Appendix, Fig. S8.

The properties of $(MnBi_2X_4)_M(Bi_2X_3)_N$ superlattices and thin films can be varied in a variety of different ways, for example by varying the pnictide fraction, applying pressure, or changing temperature. We study the efficacy of these
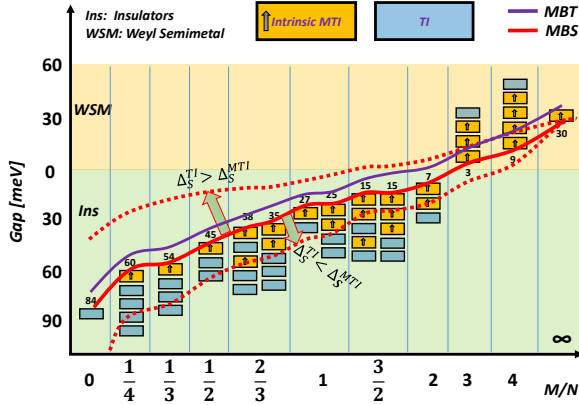
Fig. 4. Topological phase diagram of ferromagnetic-configuration $(MnBi_2X_4)_M(Bi_2X_3)_N$ superlattices *vs.* M/N. This figure was constructed by using the Dirac cone model to calculate energy bands and 2D Chern numbers as a function of k_z for all indicated superlattices. Weyl semimetal superlattices are placed in the orange region of the phase diagram and insulators in the green region. MBS energy gaps (in meV) at the Γ point are listed at the top of the corresponding superlattice icons for insulating superlattices and the bottom for the Weyl semimetal superlattices in which the gap has been inverted. The solid red (purple) line plots Γ point gaps for MBS (MBT) calculated using $\Delta_S^{MTI} = \Delta_S^{TI}$, while the dashed red lines illustrate the cases in which Δ_S^{TI} deviates from Δ_S^{MTI} by ± 10 %.

tuning knobs by constructing phase diagrams *vs.* J_S and Δ_D, as illustrated in Fig. 5, for several different stacking sequences keeping the ratio of J_S to J_D and Δ_S fixed. To limit the number of parameters we used the same values for Δ_S and Δ_D in magnetic and non-magnetic layers. The motivation for illustrating the dependence of phase on this particular subset of model parameters is that i) we expect both exchange interactions to decline with temperature as the alignment of the local moment spins decreases with increasing temperature, and ii) that we expect the van der Waals gap to narrow as pressure is applied, increasing Δ_D. The dependence of Δ_D on pressure is addressed explicitly in SI Appendix, Fig. S7. For M = 1 and N = 0 (that is for bulk $MnBi_2X_4$), the phase diagram shown in Fig. 5 (a) maps to that of the MTI/normal insulator superlattice model studied by Burkov and Balents (42). The cases of M/N = 0.5, 1 and 2 are shown in Fig. 5 (b)-(d), where the positions of MBS and MBT systems in the phase diagram are marked by red and blue dots. Although antiferromagnetic $MnSb_2Te_4$ is a trivial insulator, unlike MBT, according to DFT calculations(47) and in agreement with our results, ferromagnetic $MnSb_2Te_4$ is a Weyl semimetal accroding to DFT calculations shown in SI Appendix Fig. S2. The estimated model parameters are $m_F = J_S + J_D \approx 45meV$, $\Delta_S \approx 124meV$ and $\Delta_D \approx -166meV$ for $MnSb_2Te_4$ and thus it should lie between that of MBT and and MBS in the phase diagram of Fig. 5.

In all cases the transition between normal insulator and Weyl semimetal states occurs at weakest exchange coupling near $\Delta_D = \Delta_S$, which marks the boundary between normal insulator and topological insulator states in the non-magnetic $J_{S/D} = 0$ limit. For the limit $\Delta_D = 0$, which corresponds to isolated layers, a phase transition from a trivial insulator to a Chern insulator state occurs when the exchange interaction exceeds Δ_S; the Weyl states emerge at smaller J_S for interior magnetic layers because both exchange interactions J_S and J_D contribute. For example for M = 1, N = 0, illustrated in Fig.

5 (a), the band energy at the Γ point is $E_\Gamma = \pm(J_S + J_D) \pm \Delta_S$, and the phase transition to the Chern insulator occurs when $J_S + J_D > \Delta_S$, that is at $J_S = \Delta_S/(1 + \delta)$ with $\delta \equiv J_D/J_S$. For the case of M = 1, N = 1 shown Fig. 5 (b), the magnetic layers are isolated so that $E_\Gamma = \pm J_S \pm \Delta_S$ and $\pm J_D \pm \Delta_S$, and there are therefore two phase transition points at $\Delta_D = 0$ one at $J_S = \Delta_S$ and one at $J_D = \Delta_S$. When the latter phase transition occurs the total Chern number per period changes from $C = 1$ to $C = 2$. At finite Δ_D quantum Hall states with different Chern numbers per period are separated by Weyl semimetal states. Fig. 5 (c) and (d) show the cases of M = 1, N = 2 and M = 2, N = 1 for which the eigenvalues in the Δ_D to 0 limit are discussed in SI Appendix and imply critical values of $J_S = \Delta_S$ for the M = 1, N = 2 case, and $J_S = \Delta_S/\sqrt{1 + \delta}, \Delta_S/\delta$ for the case of M = 2, N = 1 case. It shows that ferromagnetic $Mn_2Bi_6Te_{11}$ has large chance to be a Weyl semimetal from Fig. 5 (d).
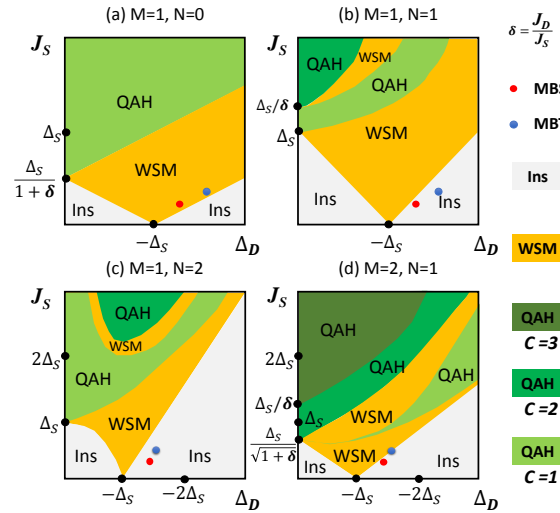

Fig. 5. Phase diagram of ferromagnetic $(MnBi_2X_4)_M$ / $(Bi_2X_3)_N$ superlattices with exchange interactions $J_S(J_D)$ and Dirac cone coupling energies Δ_D in adjacent layers and Δ_S in the same layer, where (a)-(d) are for (M,N) = (1,0)($MnBi_2X_4$), (M,N) = (1,1)($MnBi_4X_7$), (M,N) = (1,2)($MnBi_6X_{10}$), and (M,N) = (2,1)($Mn_2Bi_6X_{11}$). Increasing temperature moves points down in this phase diagram whereas applying pressure moves points to the right. The zero-temperature MBS and MBT parameters are marked by red and blue dots. From (d) it shows that ferromagnetic $Mn_2Bi_6Te_{11}$ has large chance to be a Weyl semimetal.

Discussion

The coupled Dirac cone model developed here provides an excellent qualitative description of $MnSb_xBi_{2-x}X_4$ (MPX) layered van der Waals materials in both thin film and bulk crystal limits. The simplified Dirac cone model has the advantage that it can readily be used as a platform to address the influence of gating, disorder, and external magnetic fields, all relevant perturbations that are not easily accounted for using *ab initio* approaches. It can also help explain trends across the material family, and simplify theories of systems with less translational symmetry (films that are many layers thick or bulk crystals with complex stacking arrangements) and theories of interaction effects. We anticipate that in both ferromagnetic and antiferromagneric thin films, gating can be used to drive transitions between insulators with different total

Chern numbers, including between quantum anomalous Hall insulators with non-zero total Chern numbers and ordinary insulators with total Chern numbers equal to zero. In bulk crystals we anticipate the simplified model will enable quantitative descriptions of the chiral magneto-transport anomaly (48, 49) of ferromagnetic states and the axion magneto-electric response of even layer antiferromagnetic states.

We have used the Dirac cone model here to explain the main trends in topological properties, namely that i) bulk antiferromagnetic MPX compounds are topological insulators, ii) bulk ferromagnetic MPX compounds are Weyl semimetals, iii) thin-film antiferromagnets are 2D Chern insulators when the number of layers is odd and exceeds a critical value and ordinary insulators otherwise, and iv) thin film ferromagnets that exceed a critical thickness are 2D Chern insulators whose Chern numbers grow and gaps decline with film thickness. We have reached these conclusions based mainly on the properties of van der Walls heterojunctions with MBT and MBS building blocks, but based on the phase diagrams in Fig. 5 they appear to be fairly robust. We have used the model to verify that it is not possible to realize Weyl semimetals by a repeated stacking of odd layer number antiferromagnets separated by non-magnetic spacers, even though they are 2D Chern insulators when isolated. To move more deeply into the topologically non-trivial part of phase diagram, the best prospect seems to be in engineering constituent layers so as to increase Δ_S or decrease $|\Delta_D|$ so that they are nearly equal in magnitude, for example by tuning the pnictide fraction.

Since the MPX compounds are antiferromagnetic in their ground states, it is necessary to apply an external magnetic field to align the moments and reach the ferromagnetic configuration. Because the antiferromagntic exchange interaction across the van der Waals gap is weak, the magnetic field needed to align the magnetic moments is relatively small (~ 5 T). The field strength necessary to align moments in layers separated by a single non-magnetic spacer layer is much smaller (~ 0.2 T). It follows that there is a broad field range in which the ground state configuration will consist of units with no spacers within which the moments are arranged antiferromagnetically, with the net spin of each unit aligned with the field. Still more complex magnetic configurations should be reachable in even weaker fields with suitably chosen stacking arrangments that include double non-magnetic spacers.

It is interesting to consider the implications of the Dirac cone model for the interpretation of photoemission experiments, which are confusing at present. Some ARPES experiments(26–28, 33), generally those using small photon energies near ~ 7 eV have not observed the surface-state gaps predicted for thick antiferromagnetic films by both DFT and by the coupled Dirac-cone model. Gapped Dirac cones were observed in higher photon energy (usually larger than 20 eV) ARPES experiments (10, 16, 18, 32), which are likely less surface sensitive. One possible explanation is that the lower energy ARPES experiments are more sensitive to the topologically protected edge states expected on the antiferromagnetic state surface at step edges where the number of layers present in the system changes. As illustrated in SI Appendix, Fig. S6, adding a layer to a MTI antiferromagnet either changes the Hall conductivity from zero to $\pm e^2/h$ or from $\pm e^2/h$ to zero. In either case topologically protected states are required by the quantized change in Hall conductivity.

Materials and Methods

1. Y Tokura, K Yasuda, A Tsukazaki, Magnetic topological insulators. *Nat. Rev. Phys.* **1**, 126–143 (2019).
2. R Yu, et al., Quantized anomalous hall effect in magnetic topological insulators. *Science* **329**, 61–64 (2010).
3. CZ Chang, et al., Experimental observation of the quantum anomalous hall effect in a magnetic topological insulator. *Science* **340**, 167–170 (2013).
4. J Wang, B Lian, SC Zhang, Dynamical axion field in a magnetic topological insulator superlattice. *Phys. Rev. B* **93**, 045115 (2016).
5. R Li, J Wang, XL Qi, SC Zhang, Dynamical axion field in topological magnetic insulators. *Nat. Phys.* **6**, 284–288 (2010).
6. RSK Mong, AM Essin, JE Moore, Antiferromagnetic topological insulators. *Phys. Rev. B* **81**, 245209 (2010).
7. I Lee, et al., Imaging dirac-mass disorder from magnetic dopant atoms in the ferromagnetic topological insulator crx(bi0.1sb0.9)2-xte3. *Proc. Natl. Acad. Sci.* **112**, 1316–1321 (2015).
8. MM Otrokov, et al., Highly-ordered wide bandgap materials for quantized anomalous hall and magnetoelectric effects. *2D Mater.* **4**, 025082 (2017).
9. S Eremeev, M Otrokov, E Chulkov, Competing rhombohedral and monoclinic crystal structures inmnpn2ch4compounds: An ab-initio study. *J. Alloy. Compd.* **709**, 172–178 (2017).
10. MM Otrokov, et al., Prediction and observation of an antiferromagnetic topological insulator. *Nature* **576**, 416–422 (2019).
11. D Zhang, et al., Topological axion states in the magnetic insulator $\mathrm{mnbi_2te_4}$ with the quantized magnetoelectric effect. *Phys. Rev. Lett.* **122**, 206401 (2019).
12. J Li, et al., Intrinsic magnetic topological insulators in van der waals layered mnbi2te4-family materials. *Sci. Adv.* **5**, eaaw5685 (2019).
13. S Chowdhury, KF Garrity, F Tavazza, Prediction of weyl semimetal and antiferromagnetic topological insulator phases in bi2mnse4. *npj Comput. Mater.* **5** (2019).
14. DS Lee, et al., Crystal structure, properties and nanostructuring of a new layered chalcogenide semiconductor, bi 2 mnte 4. *CrystEngComm* **15**, 5532–5538 (2013).
15. EDL Rienks, et al., Large magnetic gap at the dirac point in bi2te3/mnbi2te4 heterostructures. *Nature* **576**, 423–428 (2019).
16. A Zeugner, et al., Chemical aspects of the candidate antiferromagnetic topological insulator mnbi2te4. *Chem. Mater.* **31**, 2795–2806 (2019).
17. JQ Yan, et al., Crystal growth and magnetic structure of $\mathrm{mnbi_2te_4}$. *Phys. Rev. Mater.* **3**, 064202 (2019).
18. SH Lee, et al., Spin scattering and noncollinear spin structure-induced intrinsic anomalous hall effect in antiferromagnetic topological insulator $\mathrm{MnBi_2Te_4}$. *Phys. Rev. Res.* **1**, 012011 (2019).
19. B Li, et al., Competing magnetic interactions in the antiferromagnetic topological insulator mnbi2te4. *Phys. Rev. Lett.* **124** (2020).
20. MM Otrokov, et al., Unique thickness-dependent properties of the van der waals interlayer antiferromagnet $\mathrm{mnbi_2te_4}$ films. *Phys. Rev. Lett.* **122**, 107202 (2019).
21. C Liu, et al., Robust axion insulator and chern insulator phases in a two-dimensional antiferromagnetic topological insulator. *Nat. Mater.* **19**, 522–527 (2020).
22. KY Chen, et al., Suppression of the antiferromagnetic metallic state in the pressurized $\mathrm{MnBi_2Te_4}$ single crystal. *Phys. Rev. Mater.* **3**, 094201 (2019).
23. Y Deng, et al., Quantum anomalous hall effect in intrinsic magnetic topological insulator mnbi2te4. *Science* **367**, 895–900 (2020).
24. Y Gong, et al., Experimental realization of an intrinsic magnetic topological insulator*. *Chin. Phys. Lett.* **36**, 076801 (2019).
25. S Zhang, et al., Experimental observation of the gate-controlled reversal of the anomalous hall effect in the intrinsic magnetic topological insulator mnbi2te4 device. *Nano Lett.* **20**, 709–714 (2019).
26. H Li, et al., Dirac surface states in intrinsic magnetic topological insulators $\mathrm{eusn_2as_2}$ and $\mathrm{mnbi_{2n}te_{3n+1}}$. *Phys. Rev. X* **9**, 041039 (2019).
27. YJ Hao, et al., Gapless surface dirac cone in antiferromagnetic topological insulator $\mathrm{mnbi_2te_4}$. *Phys. Rev. X* **9**, 041038 (2019).
28. YJ Chen, et al., Topological electronic structure and its temperature evolution in antiferromagnetic topological insulator $\mathrm{mnbi_2te_4}$. *Phys. Rev. X* **9**, 041040 (2019).

29. J Ge, et al., High-chern-number and high-temperature quantum hall effect without landau levels. *Natl. Sci. Rev.*, nwaa089 (2020).

30. C Hu, et al., A van der waals antiferromagnetic topological insulator with weak interlayer magnetic coupling. *Nat. Commun.* **11**, 1–8 (2020).

31. L Ding, et al., Crystal and magnetic structures of magnetic topological insulators $\mathrm{mnbi_2te_4}$ and $\mathrm{mnbi_4te_7}$. *Phys. Rev. B* **101**, 020412 (2020).

32. RC Vidal, et al., Surface states and rashba-type spin polarization in antiferromagnetic $\mathrm{mnbi_2te_4}$(0001). *Phys. Rev. B* **100**, 121104 (2019).

33. P Swatek, et al., Gapless dirac surface states in the antiferromagnetic topological insulator $\mathrm{mnbi_2te_4}$. *Phys. Rev. B* **101**, 161109 (2020).

34. T Hirahara, et al., Large-gap magnetic topological heterostructure formed by subsurface incorporation of a ferromagnetic layer. *Nano Lett.* **17**, 3493–3500 (2017).

35. JA Hagmann, et al., Molecular beam epitaxy growth and structure of self-assembled bi2se3/bi2mnse4 multilayer heterostructures. *New J. Phys.* **19**, 085002 (2017).

36. SV Eremeev, MM Otrokov, EV Chulkov, New universal type of interface in the magnetic insulator/topological insulator heterostructures. *Nano letters* **18**, 6521–6529 (2018).

37. J Wu, et al., Natural van der waals heterostructural single crystals with both magnetic and topological properties. *Sci. Adv.* **5**, eaax9989 (2019).

38. RC Vidal, et al., Topological electronic structure and intrinsic magnetization in $\mathrm{mnbi_4te_7}$: A $\mathrm{bi_2te_3}$ derivative with a periodic mn sublattice. *Phys. Rev. X* **9**, 041065 (2019).

39. II Klimovskikh, et al., Variety of magnetic topological phases in the (mnbi$_2$te$_4$)(bi$_2$te$_3$)$_m$ family (2019).

40. H Zhang, et al., Topological insulators in bi 2 se 3, bi 2 te 3 and sb 2 te 3 with a single dirac cone on the surface. *Nat. physics* **5**, 438–442 (2009).

41. G Rosenberg, M Franz, Surface magnetic ordering in topological insulators with bulk magnetic dopants. *Phys. Rev. B* **85**, 195119 (2012).

42. AA Burkov, L Balents, Weyl semimetal in a topological insulator multilayer. *Phys. Rev. Lett.* **107**, 127205 (2011).

43. B Himmetoglu, A Floris, S de Gironcoli, M Cococcioni, Hubbard-corrected dft energy functionals: The lda+u description of correlated systems. *Int. J. Quantum Chem.* **114**, 14–49 (2013).

44. X Wan, AM Turner, A Vishwanath, SY Savrasov, Topological semimetal and fermi-arc surface states in the electronic structure of pyrochlore iridates. *Phys. Rev. B* **83**, 205101 (2011).

45. C Nowka, et al., Chemical vapor transport and characterization of mnbi2se4. *J. Cryst. Growth* **459**, 81–86 (2017).

46. A Burkov, Weyl metals. *Annu. Rev. Condens. Matter Phys.* **9**, 359–378 (2018).

47. B Chen, et al., Intrinsic magnetic topological insulator phases in the sb doped mnbi2te4 bulks and thin flakes. *Nat. Commun.* **10** (2019).

48. DT Son, BZ Spivak, Chiral anomaly and classical negative magnetoresistance of weyl metals. *Phys. Rev. B* **88**, 104412 (2013).

49. AA Burkov, Chiral anomaly and diffusive magnetotransport in weyl metals. *Phys. Rev. Lett.* **113**, 247203 (2014).

50. G Kresse, J Hafner, Ab initio molecular dynamics for liquid metals. *Phys. Rev. B* **47**, 558–561 (1993).

51. KB J. P. Perdew, M Ernzerhof, Generalized gradient approximation made simple. *Phys. Rev. Lett.* **77**, 3865 (1997).

MacDonald *et al.*

PNAS | **September 29, 2020** | vol. XXX | no. XX | **7**

Supplemental Materials for
"Magnetized Topological Insulator Multilayers"

Model parameters from bulk DFT calculations. We estimate the model Dirac velocity (v_D) parameters by examining the dependence of DFT band energies on $\mathbf{k}_\perp$, which are illustrated in Fig. S1. For each k_z, the model energy bands for ferromagnetic configurations are given by

$$E(\mathbf{k}_\perp, k_z) = \pm\sqrt{m^2 + (\hbar v_D \mathbf{k}_\perp)^2}, \tag{S1}$$

where $m = E(\mathbf{k}_\perp = 0, k_z)$ is the mass at k_z. The DFT results suggest that the approximation of linear Dirac dispersion is reasonable within several hundreds of meVs of the Fermi energy. The linear Dirac dispersion is hidden in the non-magnetic case by the large gaps already present at $\mathbf{k}_\perp = 0$. The resulting Dirac velocity parameters are summarized in Table S1 and lie in the range of a few times 10^5m/s, which is typical of Dirac materials.
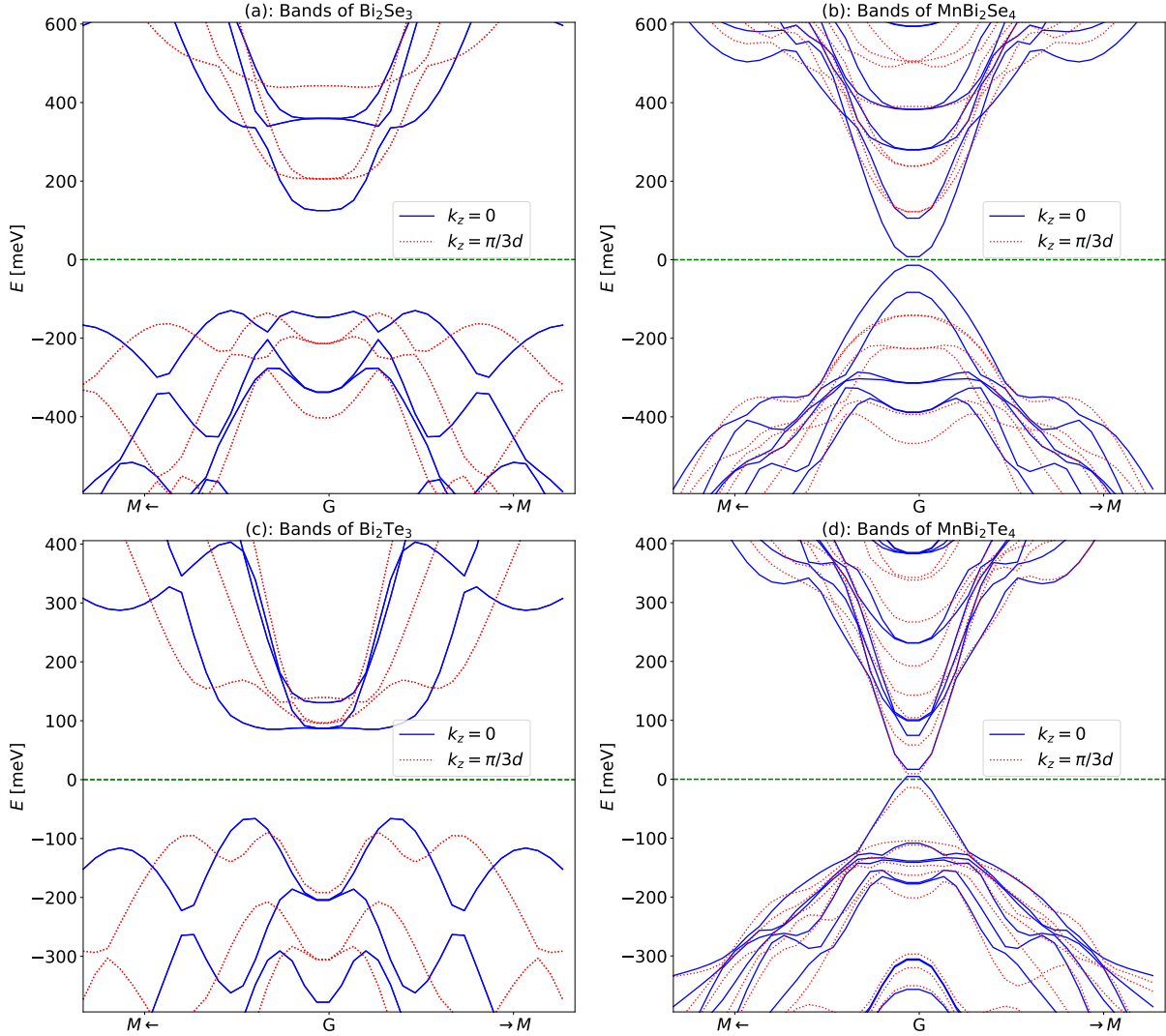

Fig. S1. Ferromagnetic configuration DFT bandstructure *vs.* $\mathbf{k}_\perp$. The solid blue lines were calculated at $k_z = 0$ and the red dashed lines at $k_z = \pi/3d$. (a): Bands of Bi$_2$Se$_3$; (b): Bands of MnBi$_2$Se$_4$; (c): Bands of Bi$_2$Te$_3$; (d): Bands of MnBi$_2$Te$_4$.

DFT band structures along the Γ to Z lines of the ferromagnetic configurations of MnBi$_2$Te$_4$, MnBi$_2$Se$_4$, MnSb$_2$Te$_4$ and MnBi$_2$Se$_2$Te$_2$ are illustrated in Fig. S2. In the last case the two middle Te atoms were replaced by Se atoms. These DFT band structure bands are folded three times since the structure repeats only after three septuple units when the microscopic stacking arrangement is taken into account. Note that MnBi$_2$Se$_2$Te$_2$ is a normal insulator, not a Weyl semimetal.

In Fig. S3 we compare DFT thin film gaps at the 2D Γ point *vs.* septuple layer number with model gaps *vs.* for both ferromagnetic and antiferromagnetic configurations. The model calculations were performed using the simplest version of the model with only the four largest parameters (J_S, J_D, Δ_S, Δ_D) which were extracted from bulk band energies at $k_z = 0$ and $k_z = \pi/d$. We have assigned a negative sign to the band gap when the thin film has an odd Chern number. Although for the gaps calculated with the model are less accurate for antiferromagnetic configurations, they do capture the trends reasonably well. In all cases, the quality of the fit to DFT can be improved by adding more model paramaeters, such as Δ_D^1, Δ_D^2, Δ_D^3 defined in the main text.

Table S1. Fermi velocities and lattice constants from DFT calculations. The range of velocities reflects a combination of anisotropy and uncertainly in the fitting procedure.

Materials	Fermi velocity (m/s)	lattice constant(Å)
$Bi_2 Se_3$	5.2×10^5 - 7.2×10^5	4.138
$MnBi_2 Se_4$	3.7×10^5 - 5.6×10^5	4.078
$Bi_2 Te_3$	3.6×10^5 - 5.1×10^5	4.383
$MnBi_2 Te_4$	3.9×10^5 - 5.5×10^5	4.407
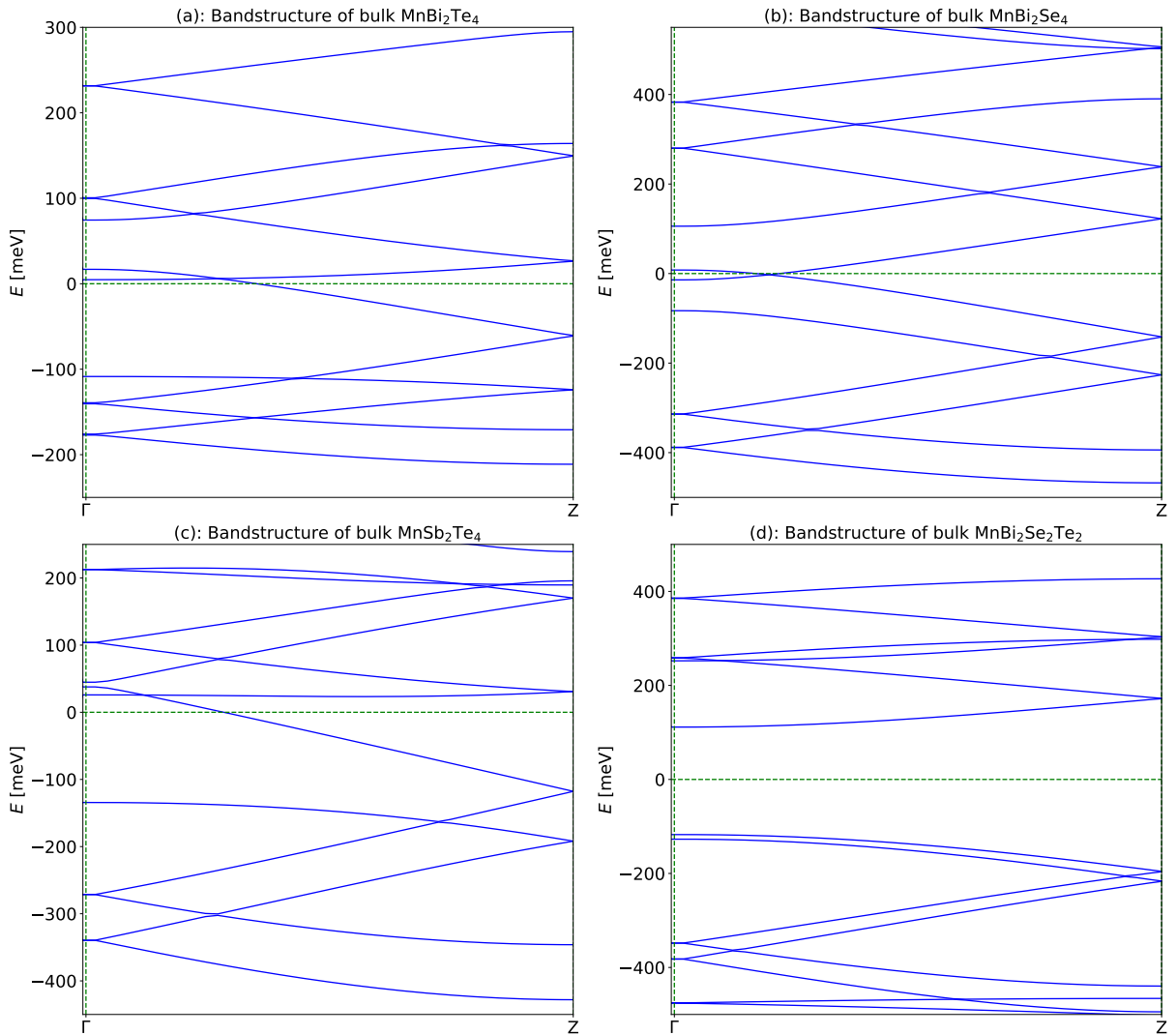
Fig. S2. Ferromagnetic configuration DFT bandstructures *vs.* $\mathbf{k}_z$ from Γ to Z at $\mathbf{k}_\perp = 0$. Since the microscopic structure repeats only after 3 septuple units, the and Z point lies at $(0,0,\pi/3d)$ where d is the septuple layer separation. (a): Bands of ferromagnetic $MnBi_2Te_4$; (b): Bands of ferromagnetic $MnBi_2Se_4$; (c): Bands of ferromagnetic $MnSb_2Te_4$(MST), in which the Bi atoms are replaced by Sb atoms, the estimation of model parameters that fit the MST DFT bandstructure are $m_F = J_S + J_D \approx 45meV$, $\Delta_S \approx 124meV$ and $\Delta_D \approx -166meV$; (d): Bands of ferromagnetic $MnBi_2Se_2 Te_2$, in which the inner two Te atoms in each septile unit are replaced by Se atoms.
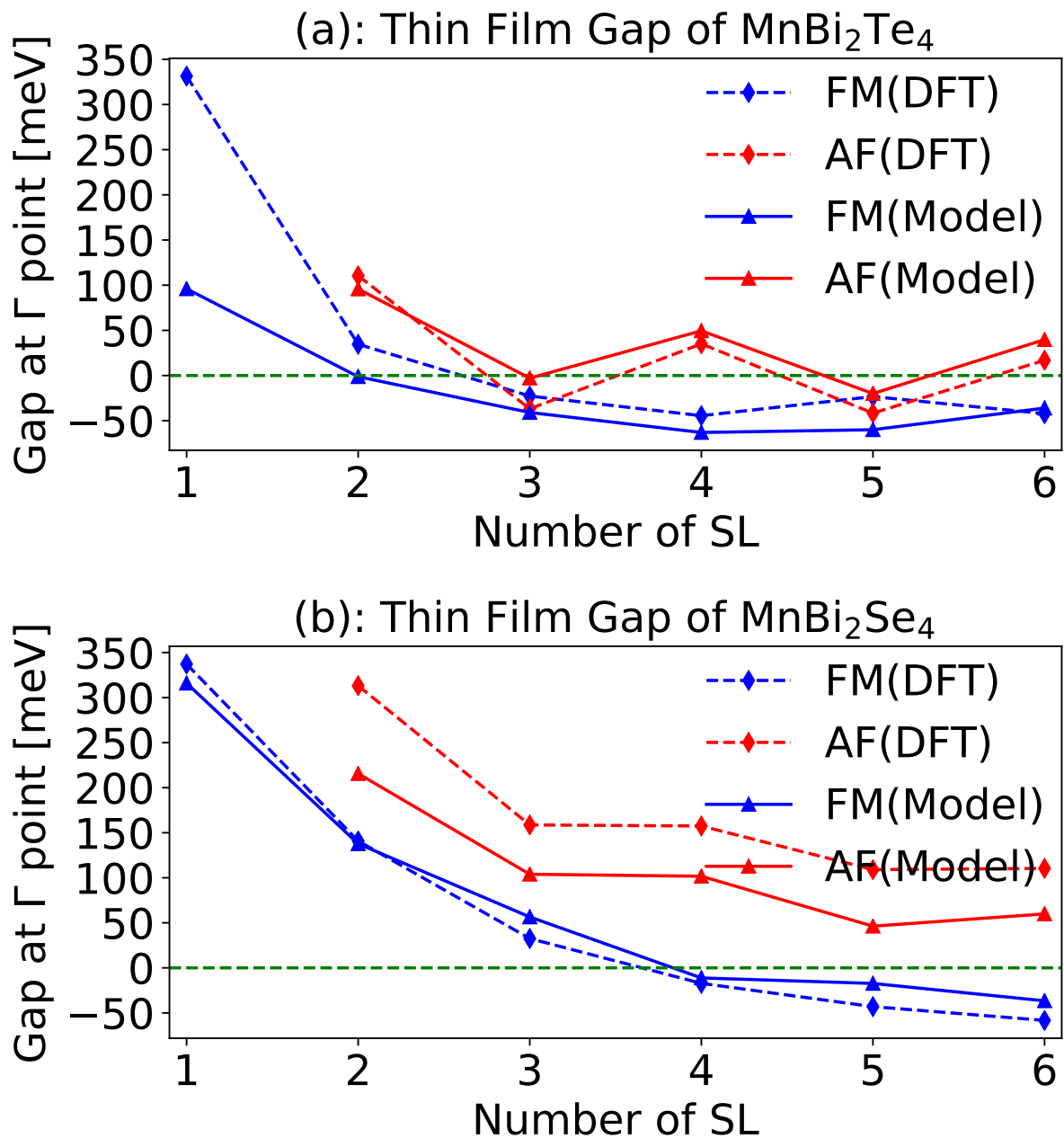
MacDonald *et al.*

Fig. S3. Comparison between model and DFT thin film 2D Γ point gaps. (a) is for $MnBi_2Te_4$ (MBT) and (b) is for $MnBi_2Se_4$ (MBS). The signs of gap are assigned based on the Chern numbers C, with negative signs applied to odd Chern numbers.
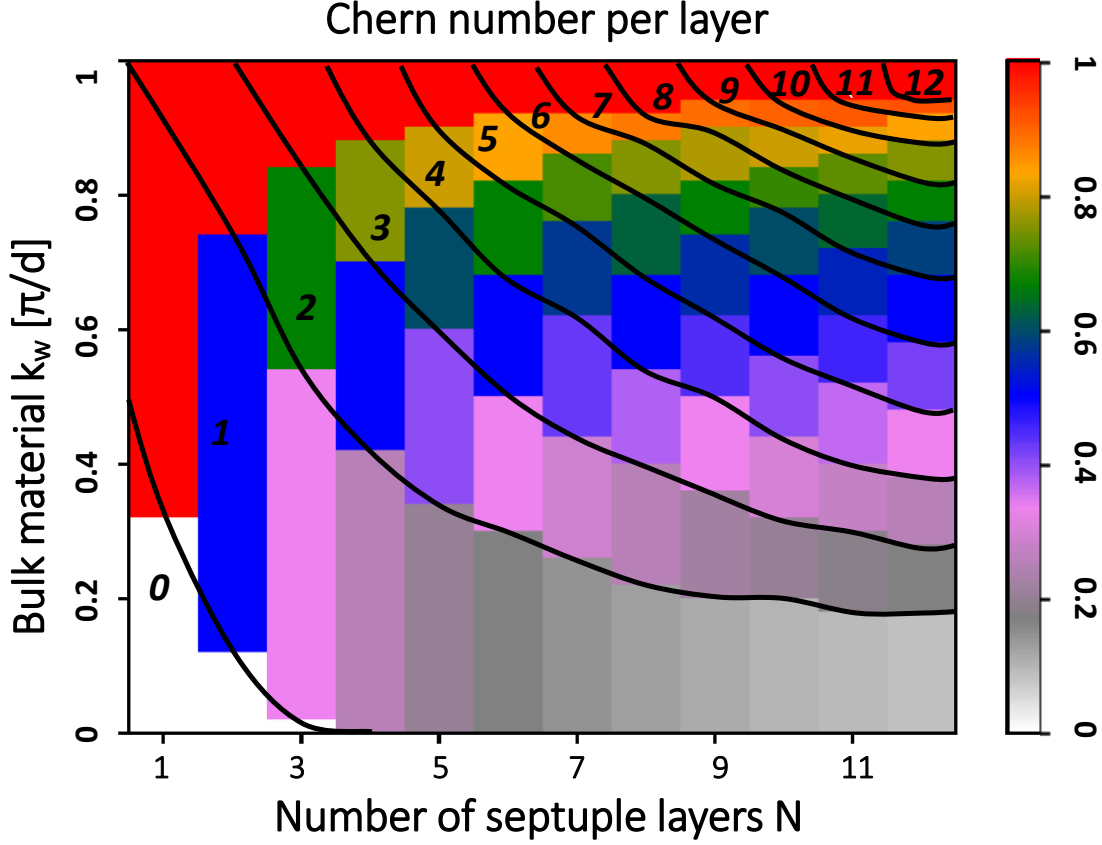
Fig. S4. Chern numbers per septuple layer (color scale) for ferromagnetic thin films *vs.* number of layers from 1 to 12 with the strength of the ferromagnetic exchange $m_F = J_S + J_D$ adjusted so as to drive the bulk Weyl momentum k_w from the Γ-point to the zone boundary. Other model parameters retain their MnBi$_2$Te$_4$ values. The Chern number per layer is obtained by dividing the total Chern number (indicated by black numbers, with black lines separating different regimes) by the number of layers. The Chern number per layer approaches its bulk value $k_w d/\pi$ as the film thickness increases.

Thin film Chern numbers. Chern numbers were calculated by integrating the Berry curvature

$$\Omega_n(\mathbf{k}) = -2 \sum_{n' \neq n} Im\left[\frac{< n|\partial_{k_x} H_{\mathbf{k}}|n' >< n'|\partial_{k_y} H_{\mathbf{k}}|n >}{(E_n - E_{n'})^2} \right] \tag{S2}$$

over k_x and k_y. The Chern number of the nth subband is

$$C_n = \frac{1}{2\pi} \int d\mathbf{k}\,\Omega_n(\mathbf{k}) \tag{S3}$$

and the total Chern number below Fermi level E_F is

$$C = \sum_{E_n < E_F} C_n = -\frac{1}{\pi} \sum_{E_n < E_F, E_{n'} > E_F} \int d\mathbf{k}\,Im\left[\frac{< n|\partial_{k_x} H_{\mathbf{k}}|n' >< n'|\partial_{k_y} H_{\mathbf{k}}|n >}{(E_n - E_{n'})^2} \right]. \tag{S4}$$

In Fig. S4 we plot thin film Chern numbers normalized per septuple layer. In this calculation we fix the Dirac cone hybridization parameters Δ_S and Δ_D to be 84 meV and -127 meV, corresponding to MBT. As shown in the main text, MBX is a Weyl semimetal when $|\Delta_D| - |\Delta_S| < J_S + J_D < |\Delta_D| + |\Delta_S|$. In Fig. S4 we have varied $m_F = J_S + J_D$ from 40 meV to 220 meV. Over this range of exchange interactions strengths the bulk Weyl point varies $k_z = 0$ to $k_z = \pi/d$ so that the bulk Hall conductivity normalized per layer,

$$\frac{\sigma_{xy}^{3D}}{d} = \frac{e^2}{h} \frac{k_w d}{\pi} \tag{S5}$$

varies from 0 to e^2/h. The corresponding thin film hall conductivities per layer are plotted in Fig. S4 for film thicknesses ranging from 1 to 12 septuple layers. Fig. S4 shows that the thin film Chern numbers per septuple layer approaches the bulk value as the film thickness increases.

Thin-film band energy trends. The evolution of thin film low-energy bands of MBX at the 2D Γ point with film thickness is illustrated in Fig.S5 for both ferromagnetic and antiferromagnetic cases and for X=Se and X=Te. For the ferromagnetic configuration, the bulk systems are Weyl semimetals. Size-quantization of the semimetal bands leads to a set of level crossings between opposite spin states at which

Chern numbers change as discussed in the bulk. For MnBi$_2$Te$_4$ these crossings occur near N = 2, 9, 15, 22, 28 *etc.*, whereas for MnBi$_2$Se$_4$ which has a smaller bulk Weyl momentum the crossings occur near N = 4, 22, *etc.*. For antiferromagnetic states, a level crossing occurs near N=3 for MnBi$_2$Te$_4$ and near N=9 for MBS. Beyond this level crossing the total Chern number is one for odd numbers of layers and zero for even numbers of layers. In the antiferromagnetic case the lowest two energy states in thick films are polarized at the surface. The crossover from normal to Chern (odd N) and axion insulator (even N) states occurs close to where the spin-splitting at the surface becomes larger than the surface-state splitting in the non-magnetic state.

In Fig. S6 (a)-(d) we illustrate how the low-energy spectrum at Γ changes upon addition of a single layer by plotting the lowest energy states of both ferromagnetic and antiferromagnetic thin films as the coupling Δ_D to the added septuple layer is increased from zero, and as the coupling Δ_S between the top and bottom surfaces of the added layer is increased from zero. In Fig. S6 (b), we illustrate the variation of low energy eigenvalues as the coupling Δ_D between an antiferromagnetic N-1 layer thin film and a single septuple layer is increased from zero to its experimental value. For N larger than the critical thickness, there is always a gap closing as Δ_D is increased, consistent with the difference in Chern number between even and odd layer number films. Once the layer has been added, however, the gap returns to the same value it had prior to layer addition if the film is sufficinetly thick; the electronic structure at the surface of a thick film is not sensitive to whether the number of layers is even or odd; that is to say that the surface electronic structures of Chern insulator and axion insulator states are identical. The difference between these states is manifested only on the side walls of finite cross-sectional area films. In the ferromagnetic case, level crossings occur only as layers are added only when the N and $N - 1$ septuple layer films have different Chern numbers.

Phase diagram vs stacking. The topological character of bulk superlattice states $(\mathrm{MBX})_M(\mathrm{BX})_N$ can usually be determined by examining the band energy ordering at the 3D Γ-point. In some limits of the model these are easily calculated analytically. In the case of $\Delta_D = 0$, for M = 1, N = 0, the energies at Γ point are:

$$E = \pm(J_S + J_D) \pm \Delta_S \qquad [S6]$$

For M = 1, N = 2, the energies at Γ point are:

$$E = \pm J_S \pm \Delta_S;$$
$$E = \frac{1}{2}\left(\pm J_D \pm \sqrt{J_D^2 + 4\Delta_S^2}\right) \quad (2\ fold\ degenerate) \qquad [S7]$$

For M = 1, N = 1, the energies at Γ point are:

$$E = \pm J_S \pm \Delta_S;$$
$$E = \pm J_D \pm \Delta_S \qquad [S8]$$

For M = 2, N = 1, the energies at Γ point are:

$$E = \pm J_D \pm \Delta_S;$$
$$E = \frac{1}{2}\left(\pm(2J_S + J_D) \pm \sqrt{J_D^2 + 4\Delta_S^2}\right) \quad (2\ fold\ degenerate) \qquad [S9]$$

For M = 3, N = 1, the energies at Γ point are:

$$E = \pm J_D \pm \Delta_S;$$
$$E = \pm(J_S + J_D) \pm \Delta_S;$$
$$E = \frac{1}{2}\left(\pm(2J_S + J_D) \pm \sqrt{J_D^2 + 4\Delta_S^2}\right) \quad (2\ fold\ degenerate) \qquad [S10]$$

For M = 4, N = 1, the energies at Γ point are:

$$E = \pm J_D \pm \Delta_S;$$
$$E = \pm(J_S + J_D) \pm \Delta_S; \quad (2\ fold\ degenerate)$$
$$E = \frac{1}{2}\left(\pm(2J_S + J_D) \pm \sqrt{J_D^2 + 4\Delta_S^2}\right) \quad (2\ fold\ degenerate) \qquad [S11]$$

For M = 5, N = 1, the energies at Γ point are:

$$E = \pm J_D \pm \Delta_S;$$
$$E = \pm(J_S + J_D) \pm \Delta_S; \quad (3\ fold\ degenerate)$$
$$E = \frac{1}{2}\left(\pm(2J_S + J_D) \pm \sqrt{J_D^2 + 4\Delta_S^2}\right) \quad (2\ fold\ degenerate) \qquad [S12]$$

For M = M, N = 1, the energies at Γ point are:

$$E = \pm J_D \pm \Delta_S;$$
$$E = \pm(J_S + J_D) \pm \Delta_S; \quad (M - 2\ fold\ degenerate)$$
$$E = \frac{1}{2}\left(\pm(2J_S + J_D) \pm \sqrt{J_D^2 + 4\Delta_S^2}\right) \quad (2\ fold\ degenerate) \qquad [S13]$$

Fig.S7 shows the gap at the Γ point of MBS from DFT vs. the strain along the $\hat{z}$-direction. This calculation shows that strains is in the range of around ±2% MBS in either direction will convert MBS from a Weyl semimetal into a normal insulator. An estimate of Δ_S and Δ_D has also been shown.

Weyl semimetal in (M,N) = (1,1) Superlattices. As shown in Fig. 4 in the maintext, stronger hybridization between surface states within the topological insulator layers trends to favor Weyl semimetal in (M,N) = (1,1) superlattices. The external magnetic field needed to realize the ferromagnetic state is expected to be dramatically lower in (M,N) = (1,1) superlattices than in a simple (M,N)=(1,0) MTI compound because of the non-magnetic spacer between magnetic layers. A natural candidate for the magnetized topological insulator layers is MnBi$_2$Te$_4$, which has the weakest same-layer surface hybridization. although MnBi$_2$Te$_4$/Bi$_2$Te$_3$ has been shown to be an insulator in Fig. 5 in the maintext, we may also consider using other non-magnetic topological insulator layers, such as Bi$_2$Se$_3$, Bi$_2$Sb$_3$, or Sb$_2$Te$_3$
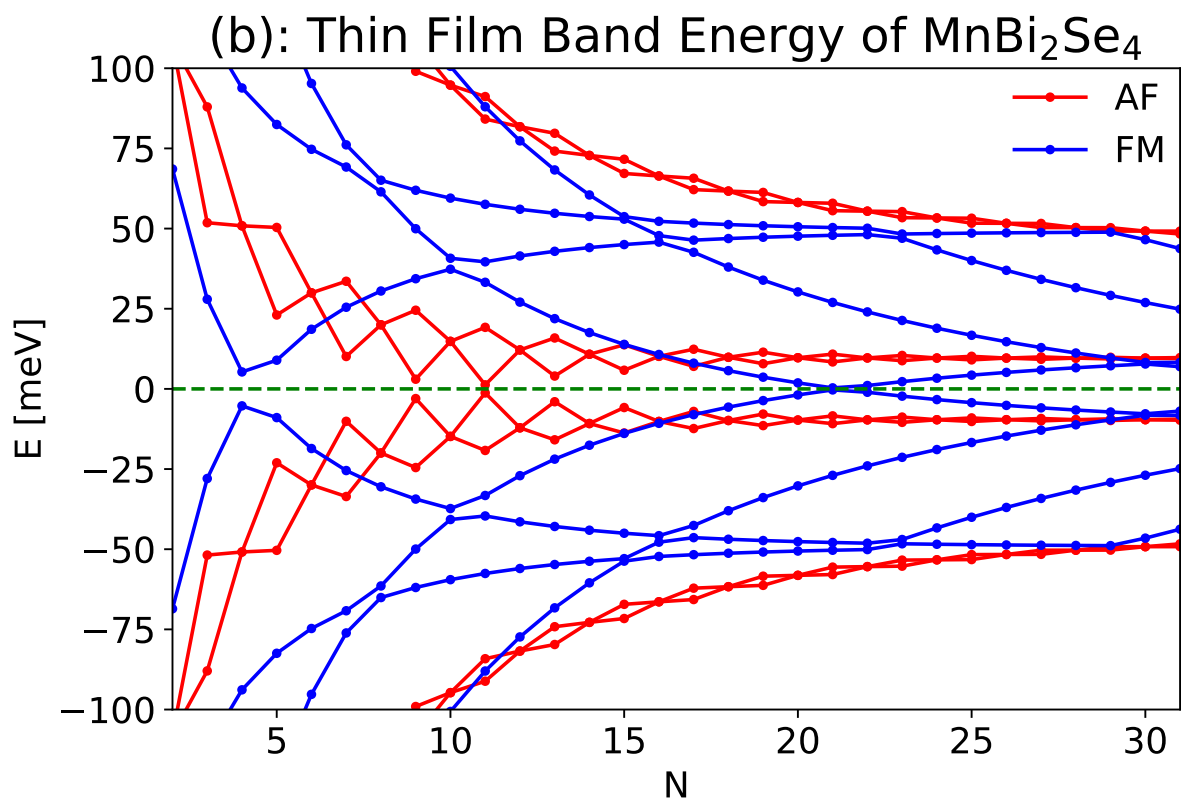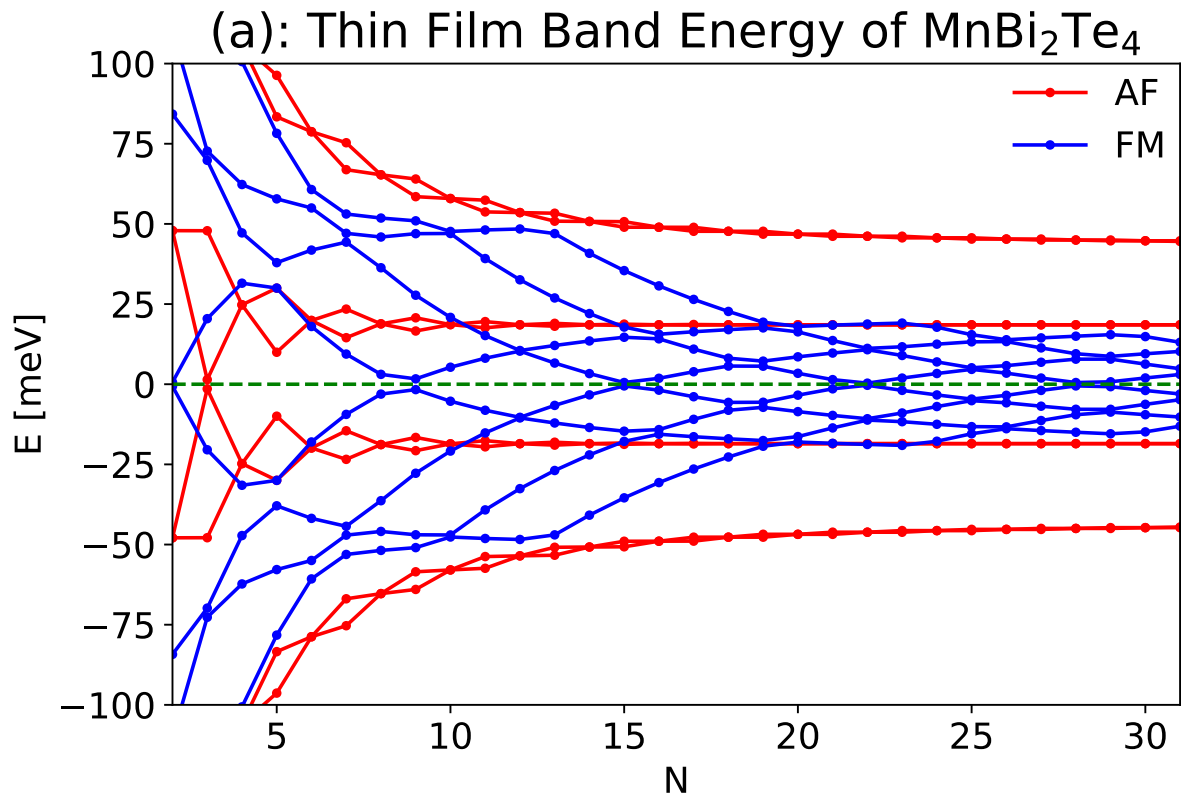
Fig. S5. The eight 2D Γ-point band energies closest to the Fermi level of neutral thin films of $MnBi_2X_4$ (MBX). The red solid lines are for the case of antiferromagnetic configurations and the blue solid lines for the case of ferromagnaetic configurations. (a): Band energies vs number of layers for $MnBi_2Te_4$ (MBT); (b): Band energies vs number of layers for $MnBi_2Se_4$ (MBS).
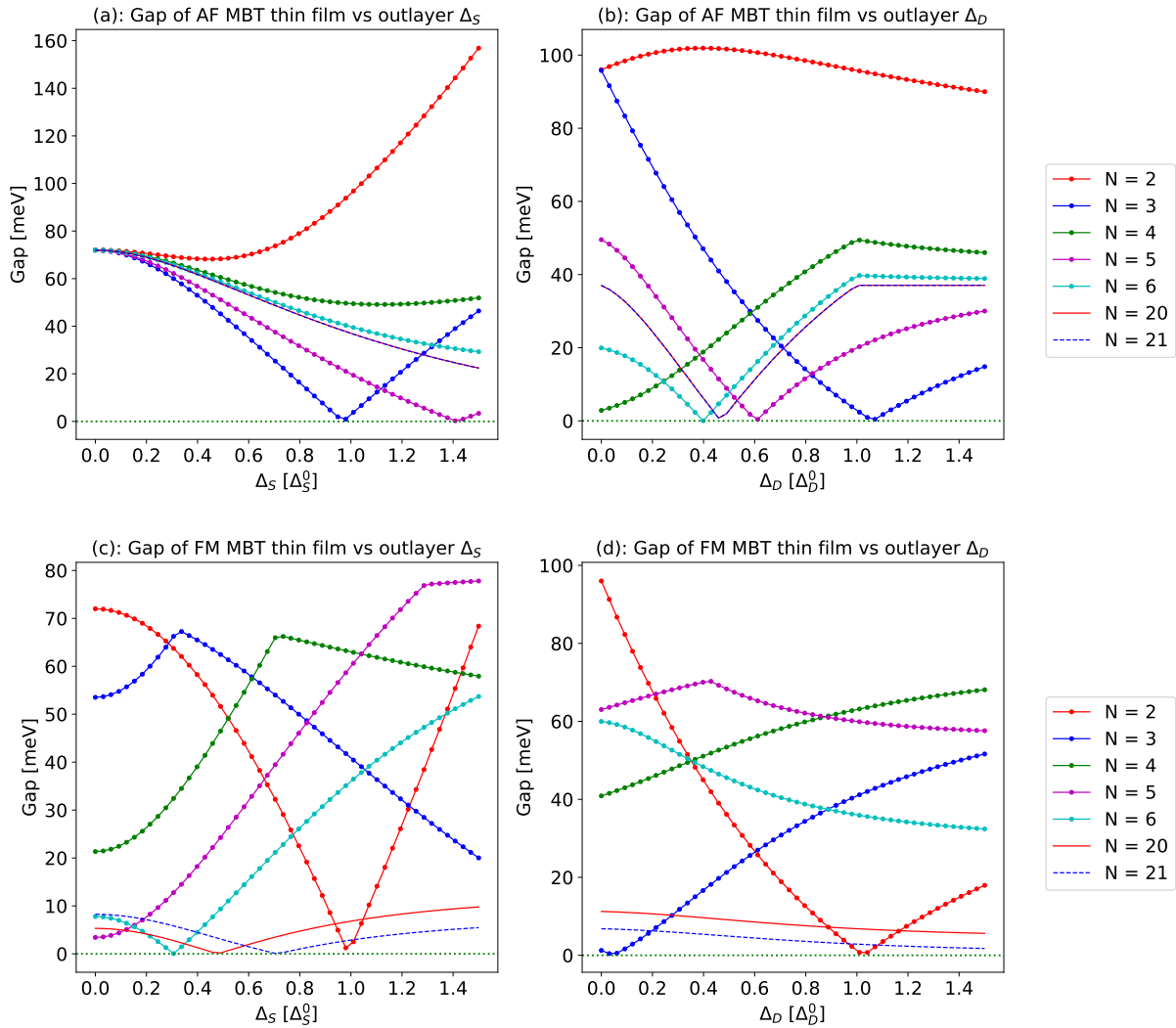
Fig. S6. Gap *vs.* coupling to added Dirac cones. (a): 2D Gap at the Γ point for antiferromagnetic MnBi$_2$Te$_4$ (MBT) thin film *vs.* the coupling $\triangle_S$ between Dirac cones on top and bottom of the top layer. (b): 2D Gap at the Γ point for antiferromagnetic MnBi$_2$Te$_4$ (MBT) thin film *vs.* the coupling $\triangle_D$ between an N-1 septuple layer film and the top septuple layer. (c): 2D Gap at the Γ point for ferromagnetic MnBi$_2$Te$_4$ (MBT) thin film *vs.* the coupling $\triangle_S$ between Dirac cones on top and bottom of the top layer. (d): 2D Gap at the Γ point for ferromagnetic MnBi$_2$Te$_4$ (MBT) thin film *vs.* the coupling $\triangle_D$ between an N-1 septuple layer film and the top septuple layer.
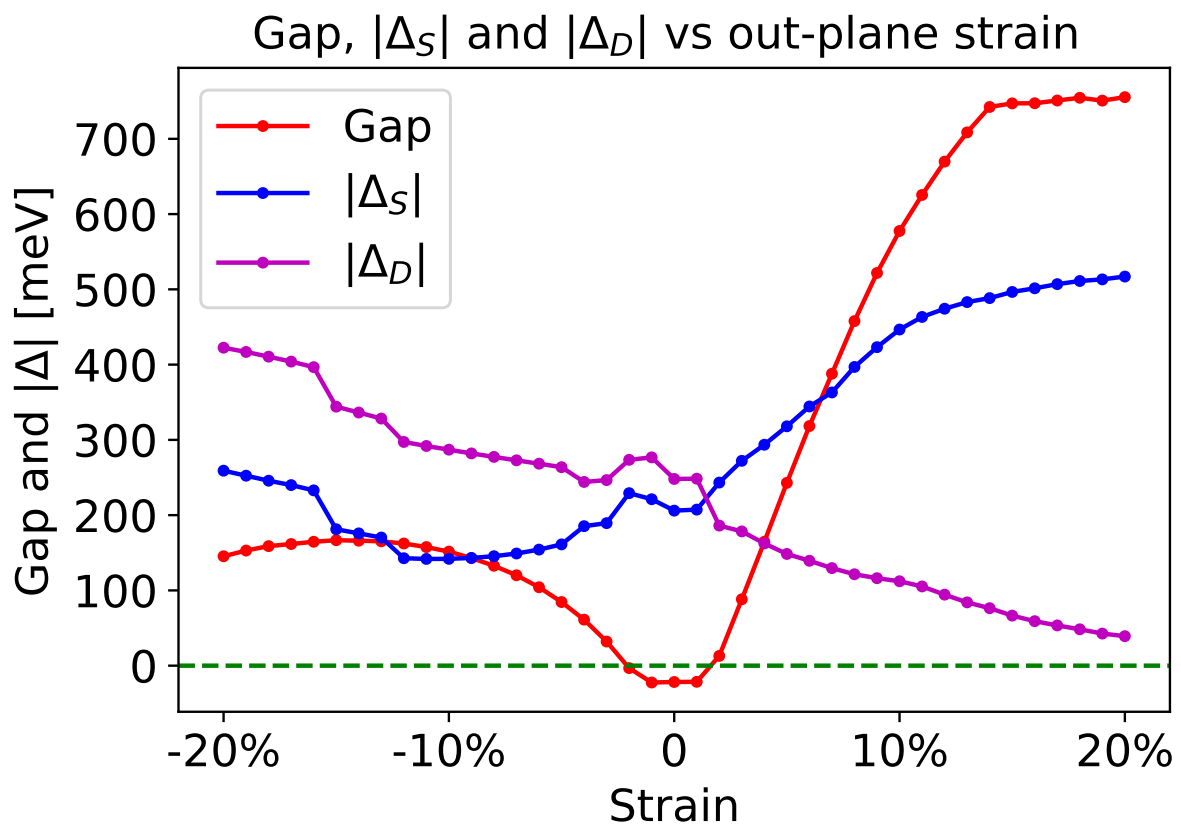
MacDonald *et al.*

PNAS | **September 29, 2020** | vol. XXX | no. XX | **7**

Fig. S7. Gap at the Γ point of MBS and the estimated values of Δ_S and Δ_D from DFT *vs.* strain along $\hat{z}$-direction.

as illustrated in Fig. S8 (e). Since these alternatives all contain one atom with a smaller radius than that in Bi_2Te_3, a smaller lattice constant is expected, thus also a stronger hybridization between same-layer surface states.

In Fig. S8 (a) the gap of a $MnBi_2Te_4/Bi_2Se_3$ superlattice at the Γ point calculated from DFT is plotted vs. variations of van der Waals spatial gap (illustrated in Fig. S8(b)) for different lateral lattice constant choices. The red curve retains the lattice constant of MBT, the green curve uses the lattice constant of Bi_2Se_3 and the blue curve uses the average lateral lattice constant. If we keep the lattice constant of $MnBi_2Te_4$, the superlattice is a Weyl semimetal. The bandstructure is shown in Fig. S8 (c). Note that a localized state appears in the Dirac-cone energy window that is not described by the Dirac cone model. These states are localized near the middle of the septuple layers and can accidentally have energies in the low-energy sector. Their position is sensitive to the on-site electron-electron interaction Mn atom +U parameter in the DFT calculations as shown in Fig. S8 (d). The results from DFT confirm the expectation from the coupled Dirac cone model, that the superlattice is a Weyl semimetal when Δ_S in the non-magnetic topological insulators layers is larger than around 105 meV, with the $\Delta_S \approx 84 meV$ in $MnBi_2Te_4$.

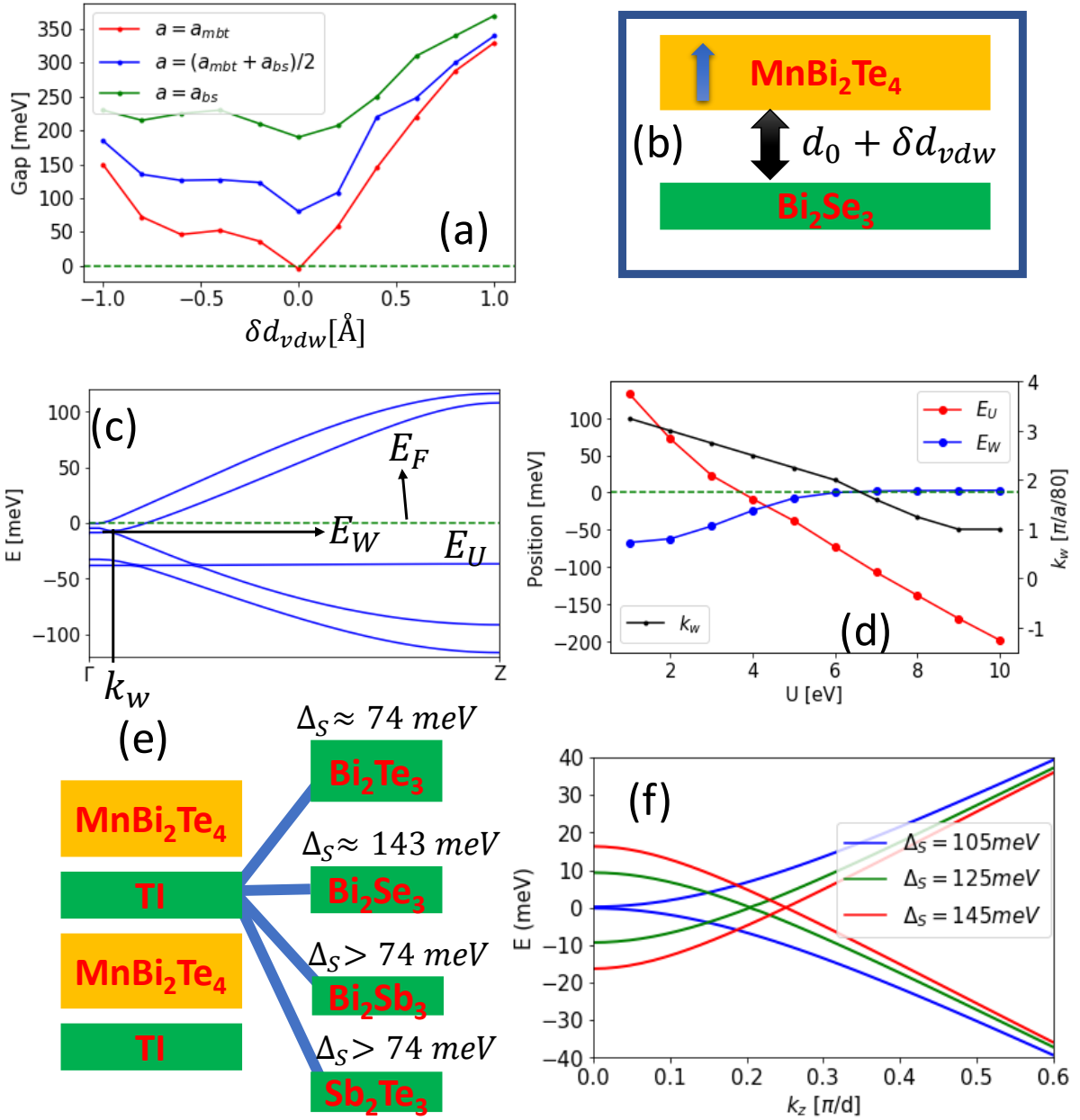**Fig. S8.** Electronic structure of superlattices with alternating septuple MBT and quintuple topological insulator(TI) layers. (a) The gap of $MnBi_2Te_4/Bi_2Se_3$ superlattices at the Γ point vs. the van der Waals spatial gap (b) at different lateral lattice constants: the red curve uses the lattice constant of MBT, and the green curve uses the lattice constant of Bi_2Se_3. (c) bandstructure calculated from DFT, which shows that a $MnBi_2Te_4/Bi_2Se_3$ superlattice with the lateral lattice constant of MBT is a Weyl semimetal and that a localized subband appears at low energies. The localized state lies outside of the Dirac-cone model Hilbert space. The energies of the Weyl point and the localized orbital are plotted as a function of the DFT +U Mn atom interaction parameter in (d). (f) illustrates Dirac cone model bandstructures calculated for MTI/TI superlattices with Δ_S parameters in the TI layers that model the topological insulator layers illustrated in (e) and the Δ_S parameter in the MTI layer fixed at 84 meV, corresponding to MBT